

Magnetism and Local Symmetry Breaking in a Mott Insulator with Strong Spin Orbit Interactions

L. Lu¹, M. Song¹, W. Liu¹, A. P. Reyes², P. Kuhns², H. O. Lee^{3,4}, I. R. Fisher^{3,4}, and V. F. Mitrović^{1,†}

¹*Department of Physics, Brown University, Providence, RI 02912, U.S.A.*

²*National High Magnetic Field Laboratory, Tallahassee, FL 32310, USA*

³*Department of Applied Physics and Geballe Laboratory for Advanced Materials, Stanford University, California 94305, USA*

⁴*Stanford Institute for Materials and Energy Sciences, SLAC National Accelerator Laboratory,*

2575 Sand Hill Road, Menlo Park, California 94025, USA

(Dated: June 30, 2021)

Study of the combined effects of strong electronic correlations with spin-orbit coupling (SOC) represents a central issue in quantum materials research. Predicting emergent properties represents a huge theoretical problem since the presence of SOC implies that the spin is not a good quantum number. Existing theories propose the emergence of a multitude of exotic quantum phases, distinguishable by either local point symmetry breaking or local spin expectation values, even in materials with simple cubic crystal structure such as $\text{Ba}_2\text{NaOsO}_6$. Experimental tests of such theories by local probes are highly sought for. Here, we report on local measurements designed to concurrently probe spin and orbital/lattice degrees of freedom of $\text{Ba}_2\text{NaOsO}_6$. We find that a novel canted ferromagnetic phase which is preceded by local point symmetry breaking is stabilized at low temperatures, as predicted by quantum theories involving multipolar spin interactions.

Introduction

Magnetic Mott insulators with strong spin-orbit coupling (SOC) represent an intriguing class of materials where various exotic quantum phases, that include spin liquid, multipolar charge order, topological insulator and semimetal, Weyl semimetal, and Axion insulator, are predicted to emerge [1–10]. SOC is a relativistic effect that in the strong regime leads to local entanglement of spin and orbital degrees of freedom. This entanglement results in drastically different physics than in cases of weak SOC. The associated emergent phenomena are particularly rich in metal oxides containing $5d$ transition-metal ions owing to the comparable magnitude of both strong electron correlations and SOC. Particularly interesting is the case of materials with a double perovskites structure [11–15], for which it has been proposed that partial lifting of degeneracy of the total angular momentum eigenstates induces a highly nontrivial multipolar exchange interactions [3, 4]. These peculiar interactions promote quantum fluctuations and thus generate novel quantum states impossible without strong SOC [3, 4, 16]. Such states include an unconventional antiferromagnet with the dominant magnetic octupole and quadrupole moments, an unusual noncollinear ferromagnet with a doubled unit cell and magnetization along the [110] axis, and biaxial spin nematic phase with quadrupolar order with preserved time-reversal symmetry stabilized in a broad intermediate temperature range above any magnetic ordering temperature. A key feature of these many-body quantum models is that significant interactions are fourth and sixth order in the effective spins, due to strongly orbital-dependent exchange.

A representative material in this class is $\text{Ba}_2\text{NaOsO}_6$, a double perovskite with Na and Os ions inhabiting alternate cation B sites, which for an undistorted structure

has a face-centered-cubic lattice, as shown in Fig. 1c. Thermodynamic and reflectivity measurements characterize this material as a $5d^1$ ferromagnetic (FM) Mott insulator with a moderate ordered moment $\sim 0.2 \mu_B$ per formula unit and $T_c \sim 6.3$ K [12, 17]. This relatively small value of the ordered moment was confirmed in μSR measurements [18]. Taking SOC into account, the anticipated ground state for a perfectly cubic point symmetry is $J_{\text{eff}} = \frac{3}{2}$. Yet, the magnetic entropy removed at FM transition is only $R \ln 2$ [12]. Though, the most unusual observation is that the FM state easy axis is in the [110] direction, as this does not occur in standard Landau theory for ferromagnetism in a cubic symmetry [3]. This uncommon magnetism can either be explained by the density functional theory (DFT) electronic structure calculations, that include effects of electron correlation, a strong SOC, and anisotropic exchange interaction [19]; or, by quantum models including multipolar exchange interactions arising from strong SOC [3, 20]. Moreover, quantum models identify the quadrupolar/orbital ordering, as a driving mechanism for the FM phase that develops atop it [3, 20]. This quadrupolar order is characterized by the orbital polarization that is distinct on the two sublattices. As such polarizations cannot be time-reversal conjugates, when magnetism onsets, a net ferromagnetic moment results. Moreover, because this anticipated quadrupolar ordering, that manifests in a breaking of the local cubic symmetry, onsets at higher temperature than magnetic order, many-body quantum based models also account for the missing entropy at the FM transition [12, 20] (see Supplementary Discussion 3). Experimental confirmation of the microscopic quantum models requires the observation of two effects. These comprise a structural change, that precedes magnetic order, associated with the quadrupolar ordering and local spin expecta-

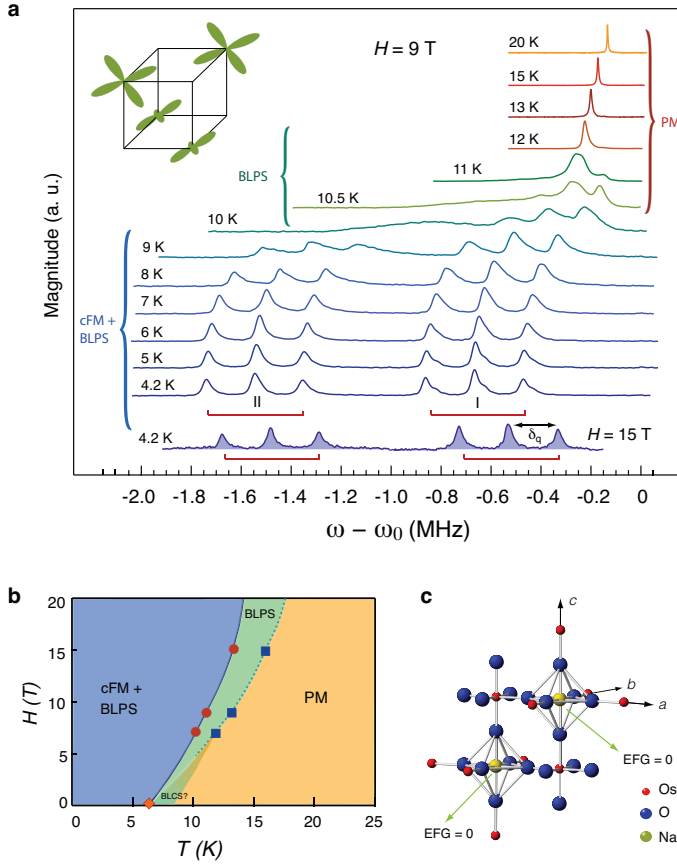


FIG. 1: Phase diagram of $\text{Ba}_2\text{NaOsO}_6$ deduced from the NMR spectra.

tion values, that differ from the average ones. Here, we report the first observation of such effects. Namely, we observe exotic local spin expectation values along with the structural changes, and infer the exact microscopic nature of the FM state and lattice distortions. We show that the FM state is in fact a type of canted ferromagnet with two sub-lattice magnetization, and that cubic symmetry breaking occurs at a temperature above the Néel temperature and it involves deformation of oxygen octahedra presumably reflecting a complicated pattern of staggered orbital order. In light of our NMR findings, we compiled the phase diagram sketched in Fig. 1b. Our results are in startlingly good agreement with recent theoretical predictions based on quantum models [3, 20]. Thus, our findings establish that such quantum models represent an appropriate theoretical framework for predicting emergent properties in materials with both strong correlations and SOC, in general.

Results

NMR Spectra. In a lattice with cubic symmetry only one Na NMR site is present, which results in a narrow single peak spectrum in the insulating paramagnetic (PM) state. Our main discovery is that, on reducing temperature, the Na NMR line undergoes a complex modification, as evident in Fig. 1a, reflecting changes in lo-

cal electron spin susceptibility and electric field gradient (EFG). That is, we deduce that this modification reflects a splitting of Na into two sites sensing different hyperfine fields due to electronic spins and breaking of the local cubic point symmetry with both sites sensing the same quadrupole frequency, related to the EFG.

To establish the sensitivity of our measurements to putative lattice distortions, orbital order, and magnetism, we first inspect the temperature (T) dependence of ^{23}Na NMR spectra in $\text{Ba}_2\text{NaOsO}_6$. These ^{23}Na spectra reveal the distribution of the hyperfine fields and the electronic charge and are thus a sensitive probe of both the electronic spin polarization (local magnetism) and charge distribution (orbital order and lattice symmetry). Temperature evolution of ^{23}Na NMR spectra is plotted in Fig. 1a. For $T > 12\text{ K}$, the spectrum consists of a single narrow NMR line, evidencing the PM state. Below 13 K, the NMR line broadens and splits into multiple peaks indicating onset of significant changes in the local symmetry, thereby producing EFG, that is asymmetric (non-cubic) charge distribution. Below 10 K, the ^{23}Na spectra clearly split into 6 peaks, that is two sets of triplet lines, labeled as I and II in Fig. 1a, that are well separated in frequency.

Two magnetic sites. Broadly speaking, the emergence of these two sets of triplets indicates appearance of two distinct magnetic sites, *i.e.* two nuclear sites that sense two different local fields, in the lattice. In a field of 9 T, the transition to the LRO state onsets in the vicinity of 10 K, which is significantly higher than the transition temperature observed in low field thermodynamic measurements in [12]. Our data measured at the different applied magnetic fields indicate that the transition temperature increases with the increasing field, confirming the magnetic nature of the transition (see Supplementary Note 2). The line shape and the fact that the two sets of triplet lines, I and II, are well separated in frequency implies that the low temperature LRO magnetic state is commensurate. Furthermore, both sets of lines are shifted to frequencies below that of spectra in the PM state. This demonstrates that the net local magnetic fields on both Na sites are of the same sign indicating that the LRO order is likely ferromagnetic.

Point symmetry breaking and EFG. Besides the splitting into sets I and II, that reflects the appearance of two distinct magnetic sites in the low T phase, we observe additional splitting of each set of the spectral lines into three peaks. Moreover, as visible in Fig. 1a, the additional splitting is discernible at temperatures higher than that for the onset of LRO state, apparent in emergence of sets I and II. This splitting, labeled as δ_q in Fig. 1a, originates from quadrupole interaction, implying changes in local charge distribution induced by modifications of electronic orbitals and/or local lattice symmetry.

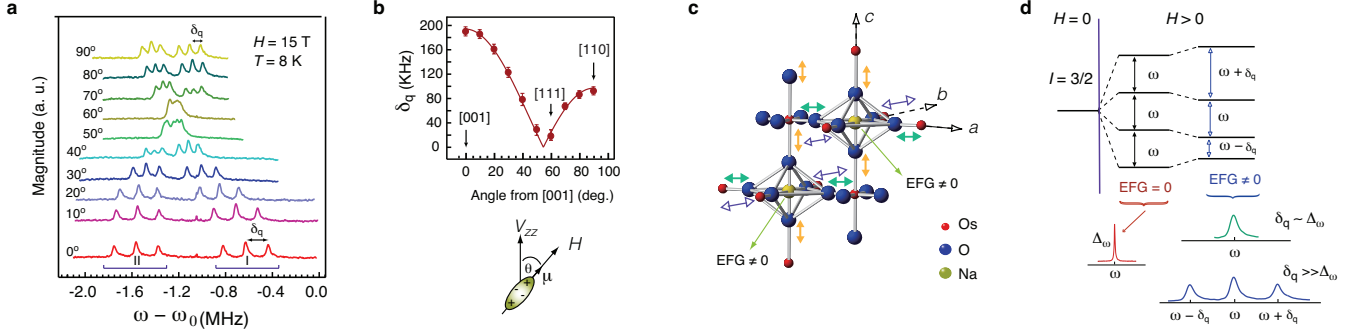


FIG. 2: Local cubic symmetry breaking in the ordered phase.

For nuclear sites with spin $I > 1/2$, such as ^{23}Na with $I = 3/2$, and non-zero EFG, quadrupole interaction between nuclear spin and EFG splits otherwise single NMR line to $2I$ lines, as illustrated in Fig. 2d. Thus, ^{23}Na spectral line splits in three in the presence of non-zero EFG. Nonetheless, for small finite values of the EFG three peaks are not necessarily discernible, in which case significant line broadening can only be observed, as depicted in Fig. 2d. At sites with cubic point symmetry the EFG is zero (see Supplementary Note 5), as is the case for Na nuclei in the high temperature PM phase. Therefore, the observed line broadening and subsequent splitting of the Na spectra into triplets, in the magnetically ordered phase, indicates breaking of the cubic point symmetry, caused by local distortions of electronic charge distribution. These distortions, marking the broken local point symmetry (BLPS) phase, occur above the transition into the magnetic state, as depicted in Fig. 1b. To confirm this finding, we measured low T spectra as a function of strength and orientation of the applied magnetic field, as we describe next.

Specifically, we examine δ_q , the average separation between two adjacent quadrupolar satellite lines, as a function of strength (H) and orientation (\mathbf{H}) of the applied magnetic field. The size of δ_q is proportional to the magnitude of the EFG and the square of the spin operator (\hat{I}_z) projected along the principal axis of the EFG (V_{zz}) (see Supplementary Note 5). In strong applied field, as is the case in our experiment, the size of δ_q is controlled by the projection of \hat{I}_z^2 along \mathbf{H} , proportional to the $\cos^2(\theta)$ of the angle θ between \mathbf{H} and V_{zz} , as shown in Fig. 2b. Evidently, δ_q is at its maximum for \mathbf{H} applied in the direction of V_{zz} , which in our experiment corresponds to [001] direction. Therefore, if the splitting δ_q originates from quadrupole interactions, δ_q should remain constant as strength of the the applied field is changed and should follow $|(3\cos^2\theta - 1)/2|$ function of θ as its orientation is varied [21]. We compare δ_q in fields ranging from 7 T to

15 T at 4 K, deep in the LRO phase (see Fig. 1a). Comparison reveals that δ_q varies by less than 2 %, which is of the order of the error bars. Furthermore, we measured the spectra at 15 T and 8 K as a function of the of the angle (θ) between \mathbf{H} and [001] crystalline axis as plotted in Fig. 2a. The angle dependence of the splitting δ_q is displayed in Fig. 2b. It indeed follows the exact functional dependence expected for the δ_q originating from quadrupole interactions. Both the observed insensitivity of δ_q to the strength of the magnetic field and its dependence on θ indicate that δ_q splitting originates from structural/orbital distortions for which the principal axes of the EFG coincide with those of the crystal (see Methods). Moreover, the insensitivity of δ_q to the strength of the magnetic field rules out the possibility that the detected distortions originate from trivial magnetostriction effects on the crystal. Our finding, that structural distortion is present in the LRO phase, is in contrast to the predictions made by the first-principles DFT calculation [19, 22]. This is important in so far that it clearly shows that quantum models based on complex multipolar interaction generating high-order spin exchange is consistent with the observed nature of emergent phases in Mott insulators with the strong SOC [3, 20].

Lattice distortions and orbital order. To resolve the microscopic nature of the observed lattice distortions and determine their magnitude, we performed detailed numerical calculations of the EFG, and thus δ_q , based on the point charge approximation [21] (see Supplementary Note 5). We found that our observation, revealing equal δ_q on two magnetically inequivalent Na sites, can be best explained by a scenario involving distortions of the O^{2-} octahedra, surrounding Na^+ ions as depicted in Fig. 2c. In this scenario, one structurally distinct Na site in non-cubic environment is generated. As it results from our calculations, distortions that generate orthorhombic local symmetry at the Na site are required to account for both the amplitude of the detected splitting ($\delta_q \approx 190 \text{ kHz}$)

and its dependence on the field orientation. Thus, in the ordered phase, our observations are explained by the orthorhombic distortions that comprise of dominant deformations along [001] and one of the crystalline axis in the (110) plane. Even though we find several possible distortions which can induce the observed splitting, we emphasize that they all involve a symmetry-lowering transition to an orthorhombic point symmetry in the LRO phase. Considering the observed amplitude of δ_q , we deduce that a typical magnitude of the distortion along any particular direction in the LRO phase does not exceed 0.8 % of the respective lattice constant. Above T_c , in the BLPS phase, the width of the NMR spectra allows us to place an upper limit on distortions. We infer that the limit equals to 0.02% of the respective lattice constant, as any deformations that exceed this value would cause visible splitting of the NMR spectra in the PM state.

In the PM state, BLPS phase is characterized by significant broadening of the NMR spectra. This broadening grows rapidly on decreasing temperature towards T_c . The angle dependence of the broadening does not coincide with either that of the internal uniform or staggered fields, indicating that the broadening predominantly originates from lattice distortions. Because in the BLPS phase we do not observe well defined splitting, but rather convoluted broadening, the exact dependence of δ_q on the field orientation is unknown. Consequently, dominant tetragonal distortions along [001] direction can in principle account for the line broadening in the PM phase. Thus, the BLPS phase can be viewed as the PM phase in which the cubic point symmetry is broken by either dominant tetragonal deformations of the oxygen tetrahedra along [001] direction or orthorhombic distortions, as is the case in the LRO phase (see Supplementary Note 5 and Supplementary Discussion 1). Hence, it is possible that the solid line, indicating T_c into LRO magnetic phase, in Fig. 1b denotes symmetry lowering transition from tetragonal-to-orthorhombic phase as well.

LRO magnetic state. We emphasize that detected lattice distortions lead to only one magnetically distinct Na site. Thus, we conclude that the observed magnetically distinct Na sites (labeled as I and II in Fig. 1) must originate from the novel type of magnetism and not from lattice distortions. In order to deduce the microscopic nature of the LRO magnetism, we next discuss the temperature and field evolution of the local fields. We used the NMR shift data to infer the local uniform ($H_u = \frac{1}{2}[\langle H_I \rangle + \langle H_{II} \rangle]$) and staggered ($H_{stag} = \frac{1}{2}[\langle H_I \rangle - \langle H_{II} \rangle]$) fields, where the average is taken over the triplet I and II, as denoted (see Supplementary Notes 1 and 2). We note that H_u corresponds to the local field as determined by the first moment of the entire spectra. Temperature evolution of these local fields is displayed in Fig. 3. Well below T_c , H_u increases with increasing H , while H_{stag} (observable only by local probes) remains constant. Interestingly, both H_u and H_{stag} are of

the same order of magnitude. Presence of H_{stag} implies that the LRO state contains two-sublattice magnetization with significant antiparallel components. Such magnetization naturally accounts for the appearance of two magnetically inequivalent Na sites, that is the appearance of distinct local fields $\langle H_I \rangle$ and $\langle H_{II} \rangle$. In Fig. 4a, the internal field at the Na site in one plane consists of a sum of the four Os moments on the same layer, and thus equal magnetic moments from one sub-lattice labeled A, and two Os above/below in neighboring layers with magnetic moment pointing in a different direction (sub-lattice labeled B), and thus producing different local field than A moments at the Na site. Na nuclei in the next plane will then sense four type B and two type A Os moments. This generates two sets of inequivalent Na sites and causes the magnetic splitting in spectrum between triplet I and II, as two types of moments induce different local fields at the Na site.

Next, we inspect the local fields as the applied magnetic field was rotated in the (1 $\bar{1}$ 0) plane of the crystal, as illustrated in Fig. 4a. This is essential for ensuring that we understand what components of anisotropic magnetic susceptibility are being measured. For $H \parallel [001]$, H_{stag} , as well as $\langle H_{II} \rangle$, reaches its maximum value, while both H_u and $\langle H_I \rangle$ are at their minimum. In principle, H_u should scale as bulk magnetization (M). As evident in Fig. 4c, this is not the case here. This finding reveals that despite the fact that the net magnetization is aligned with the [110] axis, the local fields, *i.e.* spin expectation values, are not. This very fact was predicted to arise as a direct consequence of lattice distortions driven by complex interactions in this class of materials [3].

The angular dependence of the internal fields is used to deduce the exact spin orientation in the LRO phase by calculating the local H_u and H_{stag} at the Na site for a given spin orientation. The local field consists of a contributions from electronic spins at six nearest-neighbor Os ions mediated via anisotropic hyperfine interaction (Methods). By performing full lattice sum, we calculate the local fields at the Na site as the direction of the applied field is rotated in (1 $\bar{1}$ 0) plane of the crystal. We find that the model that best describes our observations, as illustrated by the solid lines in Fig. 4a, is a two-sublattice canted FM model, recently proposed in [20] and depicted

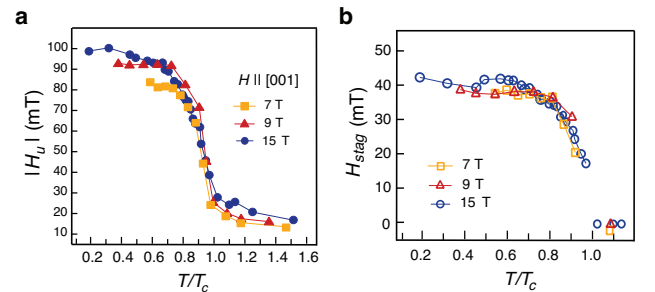


FIG. 3: Temperature dependence of the uniform and staggered fields.

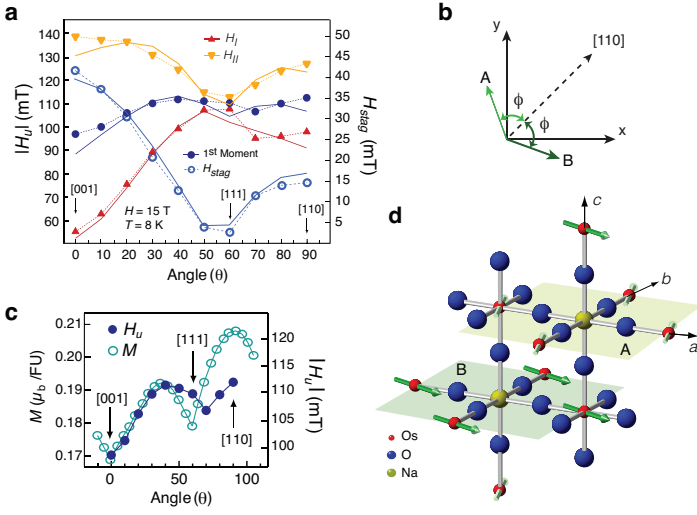


FIG. 4: Resolution of the spin orientation in the ordered phase.

in Fig. 4b. This model consists of two inequivalent sublattices with moments in each layer in the XY plane parallel to each other, forming FM order, while moments in the neighboring layers point to a different direction. Specifically, moments in two adjacent layers are symmetric about $[110]$ axis, that is they form an angle $\pm\phi$, with $[110]$ axis, as depicted in Fig. 4b and d. As direction of the applied field is varied spin-plane follows the direction of \mathbf{H} while spins remain staggered about $[110]$ axis. Moments arranged in this fashion induce an uniform field in $[110]$ direction, providing an overall shift to the NMR spectrum, and form a staggered pattern in the direction perpendicular to $[110]$. Thus, for $\mathbf{H}||[001]$ such spin arrangement generates lowest H_u and largest H_{stag} , as observed, when the canting angle ϕ exceeds 45° . The exact value of the canting angle is determined by the fitting procedure described below. The curves in Fig. 4A, are fits to the data using the simulated local fields with relative strength of the off-diagonal terms of the hyperfine coupling tensor, \mathbb{A} , (A_{ij}/A_{ii}), magnitude of the local Os moments, and the canting angle ϕ between the spins on two different sub-lattices, as fitting parameters. Constraining the diagonal terms of \mathbb{A} to be close to those found in the PM state, we find the moment of $\mu \approx 0.6 \mu_B$ and $\phi \approx 67^\circ$. Using the deduced value of ϕ and formalism in [20], we estimate the ratio of in-plane to intra-plane coupling constant to be ≈ 4 (see Supplementary Note 4). The value of the moment is in agreement with the effective moment deduced from the fit to a Curie-Weiss law in the PM state in [12]. Large canting angle ϕ explains the smaller moment detected in the FM state in bulk measurements [12, 18] due to partial cancelation of nonparallel magnetic moments. We emphasize that the symmetry of the inferred \mathbb{A} tensor reflects neither local tetragonal nor orthorhombic symmetry of the distorted O octahedra (see Supplementary Notes 3 and 4). This in-

dicates that spin-spin interactions are highly anisotropic.

Discussion

We have performed microscopic measurements on a model system of Mott insulator with strong SOC, $\text{Ba}_2\text{NaOsO}_6$. Our static NMR measurements reveal that the local cubic symmetry breaking, induced by deformation of the oxygen octahedra, precedes the formation of the LRO magnetism. We establish that LRO state is the exotic canted two-sublattice FM state, believed to be driven by the staggered quadrupolar order [3]. This is the first direct detection of such a complex quantum state with the distinct local spin expectation values. Our observation of both the local cubic symmetry breaking and appearance of two-sublattice exotic FM phase is in line with theoretical predictions based on quantum models with multipolar magnetic interactions. The fact that spin-spin interactions are indeed mediated by complex multipolar interactions, as suggested in [3], is further confirmed by our finding that the symmetry of the inferred \mathbb{A} tensor does not reflect any local symmetry of the distorted O octahedra. Moreover, it is proposed that two-sublattice magnetic structure is the very manifestation of staggered quadrupolar order and that this ordering drives the formation of LRO magnetism [3, 9]. Thus, our finding that LRO phase is a two-sublattice canted FM implies that broken cubic symmetry phase is a staggered quadrupolarly ordered phase with distinct orbital polarization on two-sublattices. In summary, our findings clearly demonstrate that microscopic quantum models with multipolar magnetic interactions are an appropriate theoretical framework for predicting emergent quantum phases in Mott insulators with the strong SOC.

Lastly, presented unique direct observation of both local cubic symmetry breaking and exotic long range ordered (LRO) magnetic state is the confirmation of the theoretical proposal that the combination of the unusual multipolar interactions, generic for spin-orbitally entangled effective spins, and/or structural transitions or quadrupolar order can lead to a highly frustrated quantum regime even for systems with spin greater than $S = 1/2$ [20]. Thus, our work illustrates that such complex quantum states might be found in other frustrated materials with both strong correlations and SOC [23, 24].

METHODS

NMR methods. The measurements were done at Brown University for magnetic field up to 9 T and at the NHMFL in Tallahassee, FL at higher fields. In both laboratories high homogeneity superconducting magnets were used. The temperature control was provided by ^4He variable temperature insert. The NMR data were recorded using a state-of-the-art laboratory-made NMR spectrometer. The spectra were obtained, at each given value of the applied field, from the sum of spin-echo

Fourier transforms recorded at constant frequency intervals. We used a standard spin echo sequence ($\pi/2 - \tau - \pi$). Shape of the spectra presented in the manuscript are independent of the duration of time interval τ . Since nuclear spin I of ^{23}Na equals to $3/2$ and at low temperatures, both Na sites (I and II) are in non-cubic environments, three distinct quadrupolar satellite lines are observed per site [21]. The shift was obtained from the frequency of the first moment of spectral distribution of set of triplet lines using a gyromagnetic ratio of $^{23}\gamma = 11.2625 \text{ MHz/T}$. The same gyromagnetic ratio was used for all frequency to field scale conversions.

Sample. High quality single crystal of $\text{Ba}_2\text{NaOsO}_6$ with a truncated octahedral morphology were grown from a molten hydroxide flux, as described elsewhere [12, 17]. Crystal quality was checked by x-ray diffraction, using a Bruker Smart Apex CCD diffractometer, which indicated that the room temperature structure belongs to the $Fm\bar{3}m$ space group [12]. NMR measurements were performed for a single crystal with a volume of approximately 1 mm^3 . The quality of the sample was confirmed by the sharpness of ^{23}Na NMR spectra both in the high temperature paramagnetic state and low temperature quadrupolar split spectra.

The sample was both zero-field and field-cooled. We did not detect any influence of the samples cooling history on the NMR spectra. Nevertheless for consistency, all results presented in the paper were obtained in field-cooled conditions. The sample was mounted to one of the crystal faces and rotated with respect to the applied field about an axis using a single axis goniometer. The rotation angle, for applied fields below 9 T, was inferred from the signal of two perpendicularly positioned Hall sensors. In addition, to ensure that data was taken with no external pressure applied, the mounted sample was placed in a solenoid coil with cross sectional area significantly larger than that of the sample. In this way, no pressure is exerted on the sample as coil contracts on cooling.

Transition Temperature: Transition temperature (T_c) from paramagnetic (PM) to low temperature ferromagnetic (FM) state was determined by examining the NMR shift and spectral line shapes, as described in detail in Supplementary Note 2. Onset temperature for breaking of local cubic symmetry, shown in Fig. 1b, was identified as temperature below which the second moment of the NMR spectral line, measuring the spectral width, increases notably as compared to that in high temperature PM phase. We point out that this temperature does not necessarily correspond to the true onset temperature for orbital ordering, which could be undetectable in our experiment due to the subtlety of the effect.

Quadrupolar Interaction and EFG: In the simplest case of a field with axial symmetry, interaction between eq , the electric field gradient (EFG), and the nucleus, with spin I and the quadrupole moment Q , is described by the Quadrupole Hamiltonian, $\mathcal{H}_Q = \frac{(eQ)(eq)}{4I(2I-1)}[3I_z^2 - I(I+1)]$. For nuclear spin $I = 3/2$, as is the case of ^{23}Na , the energy eigenstates of \mathcal{H}_Q are given by, $E = \frac{(eQ)(eq)}{4I(2I-1)}[3m^2 - I(I+1)]$. Then, the frequencies between different quadrupole satellite transitions equal,

$$\begin{aligned} \omega_{m \rightarrow m-1} &= \frac{(eQ)(eq)}{h 4I(2I-1)} [3(2m-1)] = \\ &\frac{1}{2}, \quad \text{for } | + 3/2 \rangle \rightarrow | + 1/2 \rangle \\ &0, \quad \text{for } | + 1/2 \rangle \rightarrow | - 1/2 \rangle \\ &-\frac{1}{2}, \quad \text{for } | - 1/2 \rangle \rightarrow | - 3/2 \rangle. \end{aligned} \quad (1)$$

Therefore, in a magnetic field applied along the principal axis of the EFG only 3 NMR lines (transitions) will be observed with equal splitting δ_q . In this case, the quadrupole splitting δ_q between different quadrupole satellites is simply given by $\delta_q = \frac{1}{2h}(eQ)(eq) = \frac{1}{2h}(\text{Quadrupole moment}) \times (\text{EFG})$. In our experiment equal splitting is observed between quadrupole satellites lines plotted in Fig. 1a for $\mathbf{H} \parallel [001]$ indicating that the principal axis of the EFG must be along \mathbf{H} , that is along the axis of the crystal. Further, we can estimate the value of the EFG using experimentally determined value of the splitting.

For anisotropic charge distributions, quadrupole Hamiltonian expressed in the coordinate system define by the principal axes of the EFG, is given by

$$\mathcal{H}_Q(x, y) = \frac{eQV_{zz}}{4I(2I-1)} \left[(3\hat{I}_z^2 - \hat{I}^2) + \eta(\hat{I}_x^2 - \hat{I}_y^2) \right], \quad (2)$$

where $\eta \equiv |V_{xx} - V_{yy}|/V_{zz}$ is asymmetry parameter and V_{xx} , V_{yy} , and V_{zz} are diagonal components of the EFG. Here, V_{zz} is defined as the principle component of the EFG and $|V_{xx}| < |V_{yy}| < |V_{zz}|$, by convention. In this case, the splitting is given by, $\delta_q = \frac{(eQ)(V_{zz})}{2h} \left(1 + \frac{\eta^2}{3} \right)^{1/2}$. Thus, the value of δ_q is dictated by both V_{zz} and anisotropy parameter. In the high field limit, when \mathcal{H}_Q is a perturbation to the dominant Zeeman term, the angular dependence of the splitting is given by

$$\delta_q = \frac{\Delta_q}{2} (3 \cos^2 \theta - 1 + \eta \sin^2 \theta \cos 2\phi), \quad (3)$$

where θ is the angle between the applied field \mathbf{H} and V_{zz} . As in the case of axially symmetric EFG, in the coordinate system defined by the principal axes of the EFG only 3 NMR lines (transitions) will be observed with equal splitting δ_q between them. When \mathbf{H} is rotated in such

coordinate system only 3 NMR lines are observed and the magnitude of the splitting between these lines depends only on angle θ . The fact that we observe no more than 3 lines per set (I or II) regardless of the angle between \mathbf{H} and [001] crystalline axis, as shown in Fig. 2B, indicates that \mathbf{H} was rotated in the coordinate system defined by the principal axes of the EFG. Therefore, the principal axes of the EFG must coincide with those of the crystal.

In a material with cubic symmetry, it is thus possible to stabilize three different domains, each with the principle axis of the EFG, V_{zz} , pointing along any of the 3 equivalent crystal axes. Further, local magnetic field has to be parallel to V_{zz} in each domain. The facts that the splitting is the largest for $H \parallel [001]$ (Fig. 2B), and that only 3 peaks per set are observed for $\mathbf{H} \parallel [110]$ imply that two domains are plausible in the crystal. One domain is characterized by pure uniaxial $3z^2 - r^2$ distortions where V_{zz} is in [001] direction, while the other is distinguished by $x^2 - y^2$ distortions where V_{zz} is then in the (110) plane. In the simplest case V_{zz} is parallel to [001] direction with $\eta = 0$ indicating tetragonal local symmetry. In the second case V_{zz} is aligned along [100] direction with η is of the order of 1, implying orthorhombic local symmetry. To determine the exact local symmetry, splittings δ_q obtained for \mathbf{H} rotated about one of the crystalline axis and about [110] direction have to be analyzed.

Calculation of Internal Fields: In the LRO phase, the component of the internal hyperfine field parallel to H , at an Na site, is given by $H_{\text{int}}^{\parallel} = \hat{\mathbf{h}} \cdot \sum_{\langle i \rangle} \mathbb{A}_i \cdot \boldsymbol{\mu}_i$, where $\hat{\mathbf{h}}$ is a unit vector in the applied field direction, \mathbb{A}_i is the symmetric 3×3 hyperfine coupling tensor with the i^{th} nearest-neighbor Os atom and $\boldsymbol{\mu}_i$ is its magnetic moment (see Supplementary Note 4). In the PM phase, hyperfine coupling tensor is diagonal. Due to complexity of the orbitals mediating the exchange paths, which can induce multipolar exchange interactions [3, 9] between neighboring Os spins and broken cubic symmetry, the off-diagonal elements of the hyperfine tensor A_{ij} are nonzero in the LRO phase. We point out that even if moment is not exclusively localized on Os site but the spin density is distributed to O [19], our modeling of H_{int}^i is valid. This is because the complexity of the spin density is accounted for in \mathbb{A} . For simplicity, we treat moment as $S = 1/2$ localized on Os as was done in [20]. By performing full lattice sum, we calculate the local H_u and H_{stag} at the Na site as well as Na NMR spectra, which is a histogram of the local field component projected along the applied field, as the direction of the applied field is rotated in (110) plane of the crystal.

-
- [1] Gang Chen, Leon Balents, and Andreas P. Schnyder, Spin-Orbital Singlet and Quantum Critical Point on the Diamond Lattice: FeSc_2S_4 , *Phys. Rev. Lett.* **102**, 096406 (2009).
 - [2] G. Jackeli and G. Khaliullin, Mott Insulators in the Strong Spin-Orbit Coupling Limit: From Heisenberg to a Quantum Compass and Kitaev Models, *Phys. Rev. Lett.* **102**, 017205 (2009).
 - [3] Gang Chen, Rodrigo Pereira, and Leon Balents, Exotic phases induced by strong spin-orbit coupling in ordered double perovskites, *Phys. Rev. B* **82**, 174440 (2010).
 - [4] Gang Chen and Leon Balents, Spin-orbit coupling in d^2 ordered double perovskites, *Phys. Rev. B*, **84**, 094420 (2011).
 - [5] Dmytro Pesin and Leon Balents, Mott physics and band topology in materials with strong spin-orbit interaction, *Nat Phys.*, **6**(5), 376-381 (2010).
 - [6] J. Radić, A. Di Ciolo, K. Sun, and V. Galitski, Exotic Quantum Spin Models in Spin-Orbit-Coupled Mott Insulators, *Phys. Rev. Lett.*, **109**, 085303 (2012).
 - [7] William S. Cole, Shizhong Zhang, Arun Paramekanti, and Nandini Trivedi, Bose-Hubbard Models with Synthetic Spin-Orbit Coupling: Mott Insulators, Spin Textures, and Superfluidity, *Phys. Rev. Lett.*, **109**, 085302 (2012).
 - [8] Johannes Reuther, Ronny Thomale, and Simon Trebst, Finite-temperature phase diagram of the Heisenberg-Kitaev model, *Phys. Rev. B*, **84**, 100406 (2011).
 - [9] William Witczak-Krempa, Gang Chen, Yong Baek Kim, and Leon Balents, Correlated quantum phenomena in the strong spin-orbit regime, *Annual Review of Condensed Matter Physics*, **5**(1), 57-82 (2014).
 - [10] Zohar Nussinov and Jeroen van den Brink, Compass models: Theory and physical motivations, *Rev. Mod. Phys.*, **87**, 1-59 (2015).
 - [11] Tomoko Aharen *et al.*, Structure and magnetic properties of the $S = 1$ geometrically frustrated double perovskites $\text{La}_2\text{LiReO}_6$ and Ba_2YReO_6 , *Phys. Rev. B*, **81**, 064436 (2010).
 - [12] A. S. Erickson *et al.*, Ferromagnetism in the Mott insulator $\text{Ba}_2\text{NaOsO}_6$, *Phys. Rev. Lett.*, **99**, 016404 (2007).
 - [13] Kazuhiro Yamamura, Makoto Wakeshima, and Yukio Hinatsu, Structural phase transition and magnetic properties of double perovskites Ba_2CaMO_6 ($M=\text{W, Re, Os}$), *Journal of Solid State Chemistry*, **179**(3), 605-612 (2006).
 - [14] C. R. Wiebe *et al.*, Frustration-driven spin freezing in the $S = \frac{1}{2}$ fcc perovskite $\text{Sr}_2\text{MgReO}_6$, *Phys. Rev. B*, **68**, 134410 (2003).
 - [15] C. R. Wiebe, J. E. Greedan, G. M. Luke, and J. S. Gardner, Spin-glass behavior in the $S = 1/2$ fcc ordered perovskite $\text{Sr}_2\text{CaReO}_6$, *Phys. Rev. B*, **65**, 144413 (2002).
 - [16] Tyler Dodds, Ting-Pong Choy, and Yong Baek Kim, Interplay between lattice distortion and spin-orbit coupling in double perovskites, *Phys. Rev. B*, **84**, 104439 (2011).
 - [17] Katharine E Stitzer, Mark D Smith, and Hans-Conrad zur Loye, Crystal growth of Ba_2MOsO_6 ($M=\text{Li, Na}$) from reactive hydroxide fluxes, *Solid State Sciences*, **4**(3), 311 - 316 (2002).
 - [18] Andrew J Steele *et al.*, Low-moment magnetism in the double perovskites Ba_2MOsO_6 ($M=\text{Li, Na}$), *Phys. Rev.*

- B*, **84**(14), 144416 (2011).
- [19] Shruha Gangopadhyay and Warren E. Pickett, Spin-orbit coupling, strong correlation, and insulator-metal transitions: The $J_{\text{eff}} = \frac{3}{2}$ ferromagnetic Dirac-Mott insulator $\text{Ba}_2\text{NaOsO}_6$, *Phys. Rev. B*, **91**, 045133 (2015).
 - [20] Hiroaki Ishizuka and Leon Balents, Magnetism in $S = \frac{1}{2}$ double perovskites with strong spin-orbit interactions, *Phys. Rev. B*, **90**, 184422 (2014).
 - [21] A. Abragam, *Principles of Nuclear Magnetism*. Number 216-263. Oxford University Press, 1996.
 - [22] H. J. Xiang and M.-H. Whangbo, Cooperative effect of electron correlation and spin-orbit coupling on the electronic and magnetic properties of $\text{Ba}_2\text{NaOsO}_6$, *Phys. Rev. B*, **75**, 052407 (2007).
 - [23] A. M. Cook, S. Matern, C. Hickey, A. A. Aczel, A. Paramakanti, Spin-orbit coupled $j_{\text{eff}} = 1/2$ iridium moments on the geometrically frustrated fcc lattice, *Phys. Rev. B*, **92**, 020417(R) (2015).
 - [24] Judit Romhányi, Leon Balents, and George Jackeli, Spin-Orbit Dimers and Non-Collinear Phases in d^1 Cubic Double Perovskites, Preprint at <http://arxiv.org/abs/1611.00646> (2016).

Figure Legends:

1. Phase diagram of $\text{Ba}_2\text{NaOsO}_6$ deduced from the NMR spectra. (a) Temperature evolution of ^{23}Na spectra at 9 T (and at 15 T, shaded trace) magnetic field applied parallel to [001] crystalline axis. Narrow single peak spectra characterize high temperature paramagnetic (PM) state. At intermediate temperatures, broader and more complex spectra reveal the appearance of electric field gradient (EFG) induced by breaking of local cubic symmetry. Splitting into 2 sets of triplet lines (labeled as I and II), reflecting the existence of two distinct magnetic sites in the lattice, is evident at lower temperatures. Zero of frequency is defined as $\omega_0 = ^{23}\gamma H$. Abbreviation: PM, paramagnetic; BLPS, broken local cubic symmetry; and, cFM, canted ferromagnetic. The charge density in the theoretically predicted quadrupolar phase [9] is sketched in the inset. (b) Sketch of the phase diagram based on our NMR measurements. Squares indicate onset temperature for the local cubic symmetry breaking, determined from our NMR data as explained in the text, in the PM phase. Circles denote T_c , transition temperature into canted ferromagnetic (cFM) phase, as deduced from the NMR data, while diamond marks T_c as determined from thermodynamic measurements in Ref. [12]. The solid line indicates phase transition into cFM state and also possible tetragonal-to-orthorhombic phase transition. The dashed line denotes cross over to the broken local point symmetry (BLPS) phase, as detected by NMR. (c) The high-temperature undistorted crystal structure of $\text{Ba}_2\text{NaOsO}_6$. In this case, point symmetry at the Na site is cubic leading to zero electric field gradient (EFG). Principal crystallographic axes are shown as well.

2. Local cubic symmetry breaking in the

ordered phase. (a) ^{23}Na spectra in low temperature ordered state as a function of the angle between the applied magnetic field and [001] crystalline axis. In this case, \mathbf{H} was rotated in the (110) plane of the crystal which contains three high symmetry directions: [001], [111], and [110]. (b) The mean peak-to-peak splitting (δ_q) between any two adjacent peaks of the triplets I and II. Error bars reflect the scattering of deduced (δ_q) values. Solid line is the fit to $|(3\cos^2\theta - 1)/2|$, where θ denotes the angle between the principal axis of the EFG (V_{zz}) and the applied magnetic field (\mathbf{H}) as depicted for nuclei spins $I = 3/2$ with magnetic moment μ (see Supplementary Note 5). (c) Schematic of a proposed lattice distortion involving the O^{2-} ions. The distortion breaks cubic symmetry at the Na site giving rise to finite electric field gradient (EFG). Different types and colors of double arrows illustrate unequal magnitude of oxygen displacements. Displacements along different axes can comprise either from compression or elongation of the oxygen bonds (see Supplementary Note 5). Depicted distortion magnitude is not to scale with the distance between nearest neighbor Os atoms, and is amplified for clarity. (d) Schematic of the energy levels of a spin-3/2 nucleus in a finite magnetic field and in the presence of quadrupolar interaction with EFG, generated by surrounding electronic charges, and resulting NMR spectra. In the absence of quadrupolar interaction spectrum consists of a single narrow line at frequency ω and of width Δ_ω . In the presence of quadrupolar interaction the centre transition remains at frequency ω , while the satellite transitions appear at frequencies shift by $\pm \delta_q$, proportional to the magnitude of the EFG. For small values of the EFG, satellite transition cannot be resolved and only line broadening is observed. Strictly speaking, there is also a broadening due to the distribution of magnitude of the EFG itself, but this is manifested only on the satellites and not on the central transition. In our case, this distribution can be neglected as all the lines show the same width.

3. Temperature dependence of the uniform and staggered fields. Absolute value of the uniform internal field, H_u , (a) and the staggered internal field, H_{stag} , (b) as a function of reduced temperature for various $\mathbf{H} \parallel [001]$. Typical error bars are on the order of a few per cent and not shown for clarity. Lines are guide to the eyes.

4. Resolution of the spin orientation in the ordered phase. (a) The magnitude of the internal field associated with triplet I (H_I) and II (H_{II}) (solid symbols), and the first moment of the entire spectrum (uniform field, H_u) as a function of the angle between the applied magnetic field and [001] crystalline axis at 8 K and 15 T. Open symbols depict the angular dependence of the staggered field, H_{stag} . Typical error

bars are on the order of a few per cent and not shown for clarity. Dotted lines are guide to the eyes. Solid lines are calculated fields from the spin model sketched in part D, as described in the text. **(b)** Schematic of the net magnetization in the XY plane in the spin model, consistent with our data and proposed in [20]. Arrows of different shades depict spins from two sub-lattices, labeled as A and B. These spins are canted by angle $\pm\phi$ with respect to [110] direction. **(c)** Comparison of the angular dependence of bulk magnetization per FU (formula unit) from Ref. [12] (open symbols) and H_u determined from our NMR measurements. **(d)** Schematic of the spin model consistent with our data and proposed in [20]. Different shades and orientation of arrows indicate distinct ionic (spin) environments on

Os site. Planes containing moments from sub-lattice A and B are shown. Lines are guide to the eyes.

Acknowledgements We would like to thank L. Balents and M. Horvatić for illuminating discussions. The study was supported in part by the the National Science Foundation (DMR-0547938 and DMR-1608760). The study at the NHMFL was supported by the National Science Foundation under Cooperative Agreement no. DMR95-27035 and the State of Florida. Work at Stanford University was supported by the DOE, Office of Basic Energy Sciences, under Contract No. DE-AC02-76SF00515.